



Seawater sea-sand engineered/strain-hardening cementitious composites (ECC/SHCC): Assessment and modeling of crack characteristics

Bo-Tao Huang^a, Jia-Qi Wu^b, Jing Yu^{c,d,*}, Jian-Guo Dai^{a,*}, Christopher K.Y. Leung^b, Victor C. Li^e

^a Department of Civil and Environmental Engineering, The Hong Kong Polytechnic University, Hong Kong, China

^b Department of Civil and Environmental Engineering, The Hong Kong University of Science and Technology, Hong Kong, China

^c School of Civil Engineering, Sun Yat-Sen University, Guangzhou 510275, China

^d Southern Marine Science and Engineering Guangdong Laboratory, Zhuhai 519082, PR China

^e Department of Civil and Environmental Engineering, University of Michigan, Ann Arbor, USA

ARTICLE INFO

Keywords:

Engineered cementitious composite (ECC)
Strain-hardening cementitious composite (SHCC)
Seawater
Sea-sand
Non-corrosive reinforcement
Crack characteristics
Crack assessment
Probabilistic modeling

ABSTRACT

Seawater sea-sand Engineered Cementitious Composites (SS-ECC) is a new version of ECC for marine constructions facing the scarcity of freshwater and river/manufactured sand. This study aims to assess and model the crack characteristics of SS-ECC, which are critical for its applications with non-corrosive reinforcements. The influence of sea-sand size, fiber length and fiber dosage on the crack characteristics of SS-ECC was explored. A five-dimensional representation was proposed to assess the overall performance of SS-ECC, by comprehensively considering both the crack characteristics (i.e., crack width and its variation) and the mechanical properties (i.e., compressive and tensile properties). A probabilistic model was also proposed to describe the stochastic nature and evolution of crack width, and it can be used to estimate the critical tensile strain on SS-ECC for a given crack-width limit and cumulative probability. The findings and proposed methods can facilitate the design of SS-ECC in marine and coastal structures.

1. Introduction

Engineered Cementitious Composite (ECC) is a family of micromechanically-designed fiber-reinforced cementitious composite featuring tensile strain-hardening and multiple-cracking behaviors [1–4]. ECC is also known as Strain-Hardening Cementitious Composite (SHCC) [5–7] or Ultra-High Toughness Cementitious Composite (UHTCC) [8–10] in the literature. Compared to conventional (fiber-reinforced) concrete, ECC shows significantly higher ductility under monotonic [11–13], cyclic [14,15], fatigue [16,17] and impact [18,19] loadings. In addition, special construction technologies for ECC (e.g., sprayable ECC [20,21], stay-in-place ECC formwork [22,23] and 3D-printed ECC [24,25]) have been developed for practical applications. ECC is attractive in the construction industry for achieving a safer, more durable, and more sustainable built environment.

Recently, the combined use of seawater sea-sand concrete and non-corrosive reinforcements (e.g., Fiber-Reinforced Polymer (FRP) reinforcements [26–28], stainless steel reinforcements [29–31], and steel-

FRP composite reinforcements [32,33]) in marine and coastal structures has attracted increasing attention from researchers. In marine and coastal concrete structures facing typhoon/hurricane, earthquake, and tsunami etc., structural components have to sustain complex loadings, such as monotonic, cyclic, fatigue, and impact loadings. For such concrete structures, using of ECC to replace/strengthen traditional concrete in some key components (e.g., beam-column joints [34,35]) and using ECC in functionally-graded components [36,37] can effectively enhance the mechanical performance of structures. In addition, owing to the tensile strain-hardening and multiple-cracking behaviors of ECC, replacing conventional quasi-brittle concrete by ductile ECC in FRP-reinforced components can improve the deformation compatibility between FRP and concrete, and lower the crack-induced FRP/concrete interfacial shear stress that can lead to bond splitting and cover spalling [38,39]. Therefore, the combined use of seawater sea-sand ECC (SS-ECC hereafter) and non-corrosive reinforcement such as FRP is a promising approach to fabricate sustainable, durable and resilient structural components for marine and coastal applications. Specifically, the authors

* Corresponding authors.

E-mail addresses: botaohuang@zju.edu.cn (B.-T. Huang), slxjw2@nottingham.edu.cn (J.-Q. Wu), yujing63@mail.sysu.edu.cn (J. Yu), cejgdai@polyu.edu.hk (J.-G. Dai), ckleung@ust.hk (C.K.Y. Leung), vcli@umich.edu (V.C. Li).

<https://doi.org/10.1016/j.cemconres.2020.106292>

Received 3 July 2020; Received in revised form 4 November 2020; Accepted 6 November 2020

Available online 17 November 2020

0008-8846/© 2020 Elsevier Ltd. All rights reserved.

Table 1
Mix proportions of SS-ECC (weight ratio).

Series	Mix ID	Binder		Seawater ^c	Sea-sand			Super-plasticizers ^d	PE fiber	
		Cement ^a	Silica fume ^b		≤1.18 mm	≤2.36 mm	≤4.75 mm		Length (mm)	Volume (%)
Sand-size	L12-V2.0-S1	0.8	0.2	0.18	0.3	/	/	0.0135	12	2.0
	L12-V2.0-S2	0.8	0.2	0.18	/	0.3	/	0.0135	12	2.0
	L12-V2.0-S4	0.8	0.2	0.18	/	/	0.3	0.0135	12	2.0
Fiber-dosage	L12-V1.0-S1	0.8	0.2	0.18	0.3	/	/	0.0135	12	1.0
	L12-V1.5-S1	0.8	0.2	0.18	0.3	/	/	0.0135	12	1.5
	L12-V2.0-S1	0.8	0.2	0.18	0.3	/	/	0.0135	12	2.0
Fiber-length	L06-V2.0-S1	0.8	0.2	0.18	0.3	/	/	0.0135	6	2.0
	L12-V2.0-S1	0.8	0.2	0.18	0.3	/	/	0.0135	12	2.0
	L18-V2.0-S1	0.8	0.2	0.18	0.3	/	/	0.0135	18	2.0

^a Type I 52.5 N Portland cement (BS EN 197-1:2011);

^b Class I silica fume with >92% silica dioxide by mass (BS EN 13263-1:2005);

^c As suggested in [27], the seawater was prepared by mixing freshwater and commercial sea-salt (36 g/L);

^d Polycarboxylate ether super-plasticizers (solid content).

have recently developed high-strength SS-ECC with compressive strength over 130 MPa, tensile strength over 8 MPa and tensile strain capacity about 5% [40,41].

The crack characteristics of SS-ECC is crucial for its applications in the marine and costal environment, as the crack width and distribution can affect the interaction between SS-ECC and FRP reinforcements [40] as well as the self-healing behavior [42–45] and water permeability [46–49]. Although the aforementioned studies have investigated the crack characteristics of freshwater-mixed ECC, no information is available in the literature on assessing the crack characteristics and modeling of crack width evolution (with increasing tensile strain) for SS-ECC. Additionally, it is widely known that the crack widths of ECC show a considerable level of scatter so that a probabilistic approach may be suitable to describe the stochastic crack width distribution. Specifically, several studies reported that the log-normal distribution can satisfactorily characterize the crack width distribution for conventional ECC [44–50]. On the other hand, the Weibull distribution has been widely adopted to characterize the flaw size distribution of concrete material [51–53] and some static and fatigue parameters of ECC [9,10,54]. In this study, a comparison is made between Weibull and log-normal distributions in characterizing the stochastic nature of cracks in SS-ECC. An accurate distribution function of crack widths can serve as a foundation of probabilistic treatment of crack-related mechanical and durability performance of SS-ECC.

The aforementioned knowledge gaps hinder the reliable design and wide applications of SS-ECC. This study focuses on the assessment of crack characteristics and modeling of crack width evolution in SS-ECC with the following objectives. First, the effects of ingredients, including sea-sand size, fiber length and fiber dosage, on the crack characteristics of SS-ECC were systematically explored. Micromechanics and scanning electron microscopy analysis were applied to interpret the experimental findings. Second, a five-dimensional representation to assess the overall performance of SS-ECC was proposed. This representation comprehensively considered the mechanical performance (i.e., compressive strength, tensile strength, and tensile strain capacity) and crack characteristics (i.e., crack width and its variation). Third, a probabilistic model to describe the stochastic nature and evolution of crack width with increasing tensile strain for SS-ECC was developed. The applicability of the proposed model was also validated.

2. Experimental scheme

2.1. Mix proportions

Table 1 shows the three series of mixes prepared for this study. To evaluate the effects of key composition parameters on the crack characteristics, three maximum particle sizes of sea-sand (1.18 mm, 2.36 mm

Table 2
Nominal properties of polyethylene (PE) fibers.

Length (mm)	Diameter (μm)	Tensile strength (MPa)	Elastic modulus (GPa)	Density (g/cm ³)
6, 12, 18	24	3000	120	0.97

and 4.75 mm), three fiber lengths (6 mm, 12 mm, and 18 mm), and three fiber volume dosages (1%, 1.5% and 2.0% for 12-mm fiber) were considered (Table 1). In the mix IDs, taking L12-V2.0-S1 for example, “L12” refers to the fiber length (12 mm), “V2.0” refers to the fiber volume dosage (2.0%) and “S1” refers to the maximum particle size of sea-sand (1.18 mm). Specifically, the L12-V2.0-S1 was the common group for the sand-size, fiber-dosage, and fiber-length series.

Table 2 lists the nominal properties of ultra-high-molecular-weight polyethylene (PE) fibers. Table 3 lists the particle size distribution of natural sea-sand, and over 77% of the particles are coarser than 1.18 mm. Although fine sand is preferred for making ECC according to its design theory [3,55], the sand-size series in Table 1 were designed to improve the utilization ratio of the obtained sea-sand. More information on the ingredients used in this study can be found in Huang et al. [41].

2.2. Testing methods

2.2.1. Mechanical properties

The 28-day compressive strength was determined from 50-mm cubic samples under a loading rate of 0.6 MPa/s [56]. The 28-day tensile performance was measured per the JSCE’s recommendation [57] with dumbbell samples (Fig. 1) under a loading rate of 0.5 mm/min. The fracture toughness of matrix was determined from three-point bending with pre-notched beams (160 mm × 40 mm × 40 mm with a 20-mm-depth notch). The fiber/matrix frictional bond strength was obtained from the single fiber test, with the specimen shown in Fig. 2 and a loading rate of 0.2 mm/min. The results of matrix fracture toughness and single fiber test will be used in the micromechanical modeling in Section 4.4.

2.2.2. Crack characteristics analysis

Of particular interest is the crack characteristics of SS-ECC with increasing tensile strain. A 24.2-megapixel camera (Canon EOS 6D mark ii) was used to take photos every 10 s within the gauge length (Fig. 1) during tension, and the photos were correlated to the actual tensile strain value via the time record. A resolution of about 15 μm per pixel was achieved in this study. Adobe Photoshop was then used to analyze the crack widths along the central line of the specimen at various strain levels [5,58].

Table 3

Particle size distribution of natural sea-sand.

Particle size (μm)	2360–4750	1180–2360	600–1180	300–600	150–300	75–150	<75	Total
Weight ratio (%)	16.13	61.20	13.83	8.42	0.39	0.01	0.01	100.00

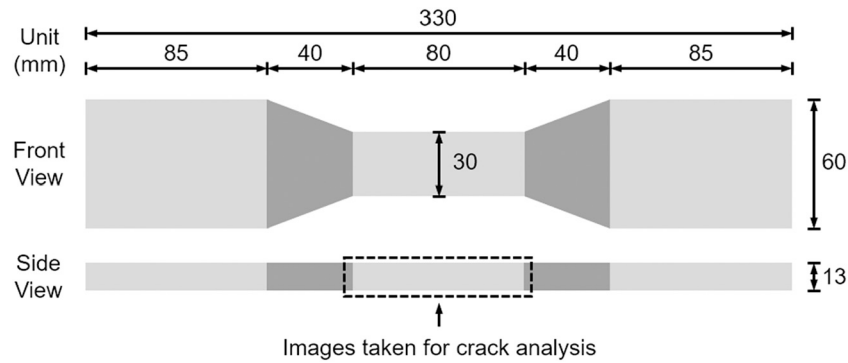


Fig. 1. Dumbbell specimen for direct tension test as recommended by the JSCE [57].

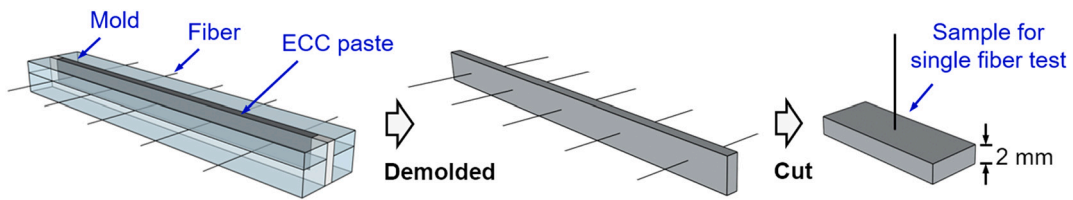


Fig. 2. Fabrication of samples for single fiber pull-out test.

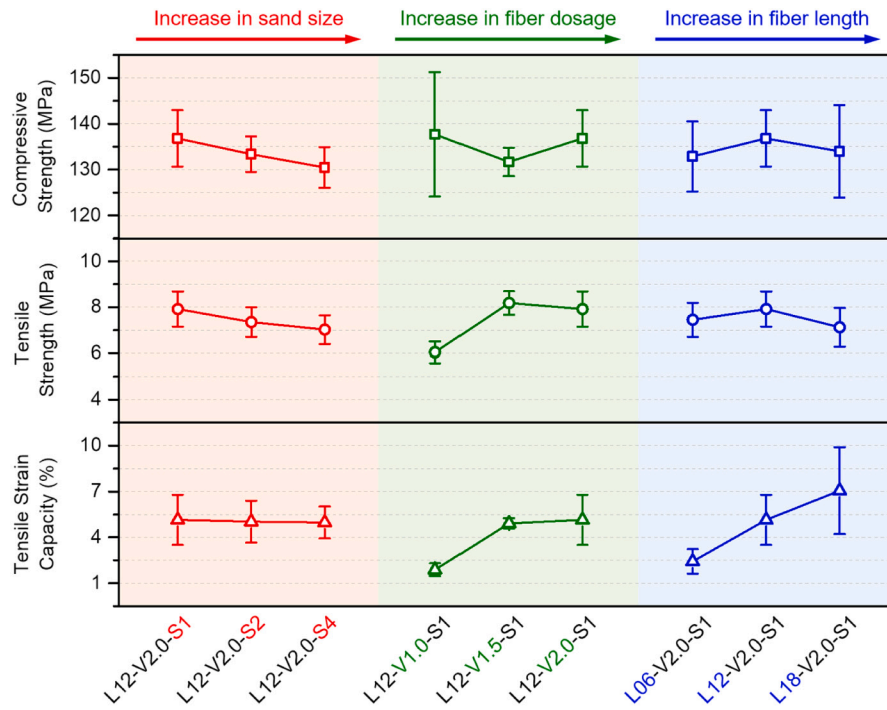


Fig. 3. Summary of compressive strength and tensile properties of SS-ECC.

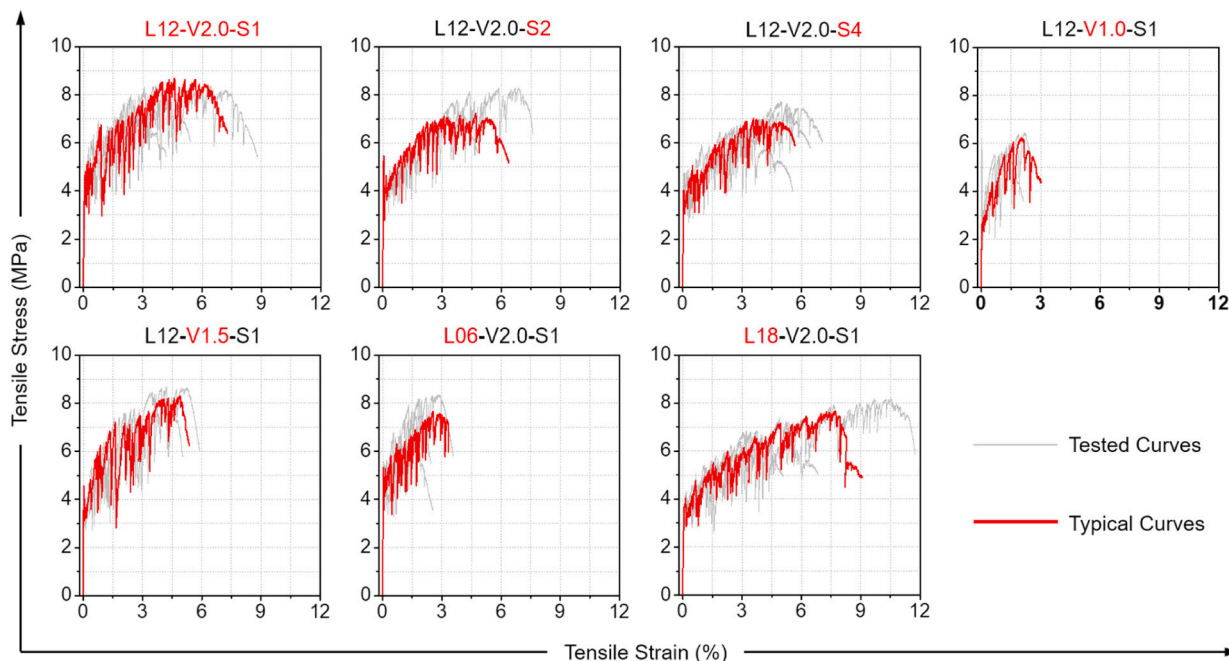


Fig. 4. Tensile stress-strain curves of SS-ECC. All mixes exhibit multiple-cracking and tensile strain-hardening performance.

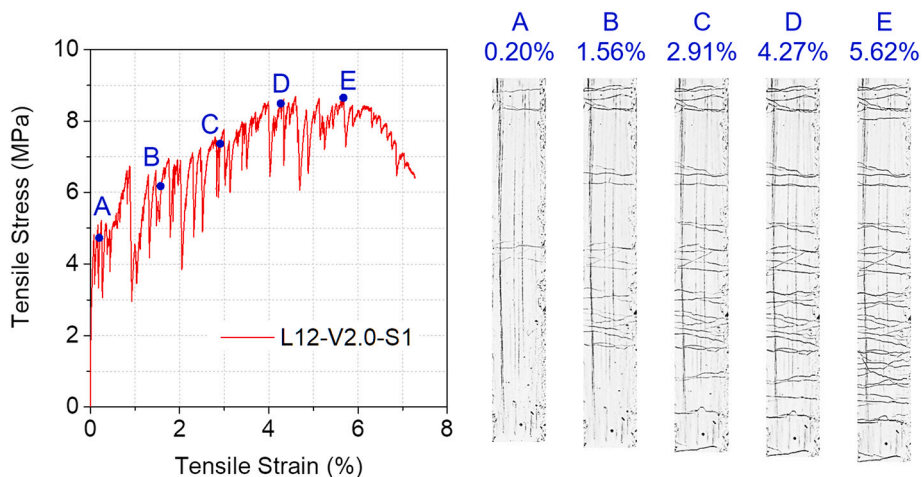


Fig. 5. Crack characteristics of SS-ECC (L12-V2.0-S1 as an example) at different tensile strain levels. The crack number increases as the tensile strain increases.

2.2.3. Fiber status after tension

To investigate the failure modes and surface morphologies of PE fibers in SS-ECC, small pieces of samples were collected from the fracture surface of the tensile specimen after testing, and then characterized by the scanning electron microscopy (SEM, JEOL-6390).

3. Compressive strength and tensile properties

Fig. 3 summarizes the compressive strength and tensile properties of SS-ECC, while Fig. 4 presents the tensile stress-strain curves. The mechanical properties are briefly summarized in this paper, and a more detailed discussion of the mechanical performance of SS-ECC can be found in a former work of the authors [41].

All the SS-ECC achieved 28-day compressive strength over 130 MPa. A larger sand size led to slightly lower compressive strength, while the fiber dosage and length had no obvious effect on the compressive strength. For the tensile performance, an increased fiber dosage from 1.0 vol% to 2.0 vol% generally led to increased tensile strength and

tensile strain capacity, which is consistent with the design theory of ECC [3]. On the other hand, a longer fiber length had no obvious effect on the tensile strength, but led to a significant increase in the tensile strain capacity, from 2.5% for 6-mm fiber to over 7% for 18-mm fiber.

In the following sections, the crack characteristics of the representative tensile curves (the red ones in Fig. 4) are analyzed and evaluated based on probabilistic approaches and microscale investigations. It should be pointed out that the representative curve in Fig. 4 is the curve closest to the average tensile performance of that specific group.

4. Crack characteristics and assessment

4.1. Crack characteristics at different tensile strain levels from experiment

The crack characteristics of SS-ECC at five tensile strain levels were investigated (from A to E). For each selected sample in Fig. 4, the strain level A is set as 0.20% reflecting the strain under the serviceability stage; the strain level E is the ultimate tensile strain reflecting the softening

Table 4
Crack numbers and distribution parameters for the selected samples.

Specimen ID	Strain (%)	Number of cracks									Weibull distribution			Log-normal distribution		
		0–15 μm	15–30 μm	30–45 μm	45–60 μm	60–75 μm	75–90 μm	90–105 μm	105–120 μm	>120 μm	λ	k	r_w	μ	σ	r_L
L12-V2.0-S1	A: 0.20	1	2	2	0	0	0	0	0	0	39.1	2.09	0.943	3.46	0.587	0.930
	B: 1.56	3	7	8	7	0	0	0	0	0	47.9	2.55	0.959	3.70	0.452	0.952
	C: 2.92	4	7	9	9	4	2	0	0	0	55.8	2.31	0.977	3.84	0.500	0.970
	D: 4.28	2	7	11	8	7	4	1	0	0	62.6	2.42	0.980	3.96	0.471	0.977
	E: 5.64	2	10	8	15	7	3	0	2	1 (150 μm)	63.7	2.49	0.975	3.98	0.486	0.970
L12-V2.0-S2	A: 0.20	1	2	1	0	0	0	0	0	0	35.8	1.86	0.946	3.35	0.663	0.935
	B: 1.45	2	4	4	4	0	0	0	0	0	47.5	2.27	0.963	3.67	0.509	0.954
	C: 2.70	3	7	6	8	2	0	0	0	0	51.6	2.31	0.967	3.75	0.505	0.960
	D: 3.95	3	7	8	7	5	1	2	0	0	58.8	2.17	0.981	3.88	0.530	0.977
	E: 5.20	3	4	13	17	7	2	2	2	0	64.1	3.04	0.967	4.02	0.378	0.966
L12-V2.0-S4	A: 0.20	1	2	1	1	0	0	0	0	0	42.8	1.69	0.974	3.51	0.692	0.968
	B: 1.38	2	7	4	5	1	0	0	0	0	63.6	3.01	0.960	4.01	0.377	0.960
	C: 2.55	2	3	9	10	4	1	2	0	0	61.8	2.94	0.967	3.98	0.388	0.965
	D: 3.73	1	1	4	13	6	5	0	3	1 (165 μm); 1 (195 μm)	77.8	3.07	0.961	4.22	0.371	0.966
	E: 4.90	0	1	6	14	8	6	6	3	1 (180 μm); 1 (270 μm)	84.7	2.90	0.975	4.29	0.389	0.979
L12-V1.0-S1	A: 0.20	0	1	0	1	1	0	0	0	0	67.0	1.72	0.972	3.96	0.739	0.959
	B: 0.66	0	0	0	0	0	1	1	0	1 (165 μm); 1 (180 μm)	156.9	2.25	0.961	4.86	0.518	0.961
	C: 1.12	0	0	0	0	1	0	0	0	1 (135 μm); 1 (165 μm); 2 (240 μm); 1 (270 μm)	211.0	1.79	0.988	5.11	0.666	0.980
	D: 1.58	0	0	0	1	0	0	0	1	1 (165 μm); 1 (210 μm); 1 (300 μm)	231.7	1.59	0.984	5.18	0.748	0.974
	E: 2.04	0	0	0	0	1	0	0	0	1 (150 μm); 1 (165 μm); 1 (180 μm); 1 (240 μm); 1 (345 μm); 1 (375 μm)	255.8	1.68	0.979	5.30	0.657	0.979
L12-V1.5-S1	A: 0.20	2	2	1	1	0	0	0	0	0	38.5	1.50	0.971	3.36	0.779	0.968
	B: 1.38	2	2	5	5	2	2	0	1	0	63.5	2.25	0.978	3.97	0.496	0.974
	C: 2.55	1	2	4	7	5	1	6	0	0	77.4	2.52	0.978	4.18	0.439	0.976
		1	2	3	6	5	5	2	3		98.2	2.14	0.991	4.39	0.522	0.991

(continued on next page)

Table 4 (continued)

Specimen ID	Strain (%)	Number of cracks									Weibull distribution			Log-normal distribution		
		0–15 μm	15–30 μm	30–45 μm	45–60 μm	60–75 μm	75–90 μm	90–105 μm	105–120 μm	>120 μm	λ	k	r _w	μ	σ	r _L
L06-V2.0-S1	D: 3.73									3 (135 μm); 2 (165 μm); 1 (180 μm)						
	E: 4.90	0	1	3	4	6	3	7	3	1 (135 μm); 2 (150 μm); 2 (165 μm); 1 (180 μm)	107.0	2.55	0.989	4.51	0.451	0.988
	A: 0.20	0	1	2	0	0	0	0	0	0	45.3	3.03	0.866	3.68	0.408	0.866
	B: 0.98	1	4	4	5	1	0	0	0	0	53.0	2.56	0.962	3.80	0.461	0.956
	C: 1.75	1	8	9	6	1	0	0	0	0	49.3	2.88	0.953	3.75	0.405	0.950
L18-V2.0-S1	D: 2.53	1	3	13	7	3	2	1	0	0	58.9	3.01	0.947	3.94	0.371	0.950
	E: 3.30	2	8	8	3	6	3	3	0	1 (240 μm)	66.0	1.85	0.981	3.95	0.618	0.981
	A: 0.20	0	2	1	0	0	0	0	0	0	39.8	2.67	0.866	3.53	0.408	0.866
	B: 2.13	1	5	7	5	3	1	0	0	0	56.2	2.57	0.971	3.86	0.455	0.969
	C: 4.05	1	3	7	4	8	3	4	1	1 (135 μm); 1 (150 μm); 1 (165 μm)	82.7	2.21	0.986	4.22	0.526	0.985
L12-V2.0-S1	D: 5.98	1	3	8	7	9	4	2	2	1 (150 μm); 1 (165 μm); 1 (180 μm); 1 (255 μm)	80.6	2.37	0.982	4.21	0.497	0.985
	E: 7.90	1	3	6	5	6	7	0	5	4 (135 μm); 1 (165 μm); 1 (180 μm); 1 (300 μm); 1 (315 μm)	97.0	1.97	0.989	4.36	0.586	0.990

point as per the JSCE’s recommendation [57]; and the strain levels B, C, and D divide the strain range between A and E into quarters. An example for the five strain levels for the selected sample of L12-V2.0-S1 is shown in Fig. 5.

For each selected sample, the crack width and number at different strain levels (from A to E) were obtained from the digital photos, and the results are summarized in Table 4. It should be noted that the step of the crack-width groups was set to be 15 μm, due to the restriction of the resolution of photos (i.e., 15 μm per pixel). The cracks with width above 120 μm are listed together in one column. Taking “1 (150 μm)” at point E of L12-V2.0-S1 for example, “1” means the number of crack and “150 μm” means the crack width.

4.2. Comparison of Weibull and log-normal distributions for crack width

In Table 4, it can be found that the crack widths of SS-ECC have considerable scatter at a given tensile strain level. In the following, the

crack width distributions of SS-ECC are fitted by both log-normal and Weibull distributions, and the accuracies of the two distributions are compared.

For the log-normal distribution, the probability density function (PDF) and cumulative distribution function (CDF) can be expressed as Eq. (1) and Eq. (2), respectively.

$$f_L(w) = \frac{1}{w\sigma\sqrt{2\pi}} \exp\left(-\frac{(\ln w - \mu)^2}{2\sigma^2}\right) \tag{1}$$

$$F_L(w) = \frac{1}{2} + \frac{1}{2} \operatorname{erf}\left(\frac{\ln w - \mu}{\sqrt{2}\sigma}\right) \tag{2}$$

where w is the crack width (variable); σ and μ are the mean value and standard deviation of the variable’s natural logarithm, respectively; and $f_L(w)$ and $F_L(w)$ are the Log-normal PDF and CDF, respectively.

For the Weibull distribution, the PDF and CDF can be expressed as

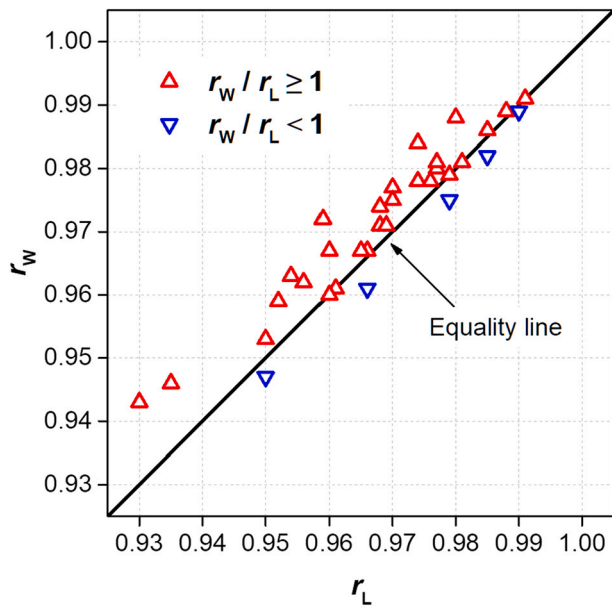


Fig. 6. The correlation coefficient of Weibull distribution r_w is greater than or equal to that of log-normal distribution r_L in most of the cases, while r_w is smaller than r_L only in 5 cases (out of 35).

Eq. (3) and Eq. (4), respectively.

$$f_w(w) = \left(\frac{k}{\lambda}\right) \left(\frac{w}{\lambda}\right)^{k-1} \exp\left(-\left(\frac{w}{\lambda}\right)^k\right) \quad (3)$$

$$F_w(w) = 1 - \exp\left(-\left(\frac{w}{\lambda}\right)^k\right) \quad (4)$$

where w is the crack width (variable); λ and k are the scale and shape parameters, respectively; and $f_w(w)$ and $F_w(w)$ are the Weibull PDF and CDF, respectively.

For the crack widths summarized in Table 4, the CDFs of Weibull and log-normal distributions were used to fit the crack width distributions at all strain levels. The fitted distribution parameters and corresponding correlation coefficients (r_w for Weibull and r_L for log-normal) are also listed in Table 4. A value of unity represents perfect fitting. The results showed that both r_w and r_L ranged from 0.866 to 0.991, which indicates that both Weibull and log-normal distributions can be used to describe the crack width distribution at various strain levels for SS-ECC. In Fig. 6, r_w and r_L are plotted together for comparison and an equality line is also presented as reference. It can be seen that r_w was greater than or equal to r_L in most of the cases, while r_w was smaller than r_L only in 5 cases (out of 35). Additionally, even in the cases showing $r_w < r_L$, the values of r_w and r_L were still very close.

Based on the above observations, it can be concluded that the Weibull distribution is more suitable than the log-normal one for fitting the crack width distributions of SS-ECC, at least for the materials studied. Therefore, the Weibull distribution is selected for further discussion in later sections.

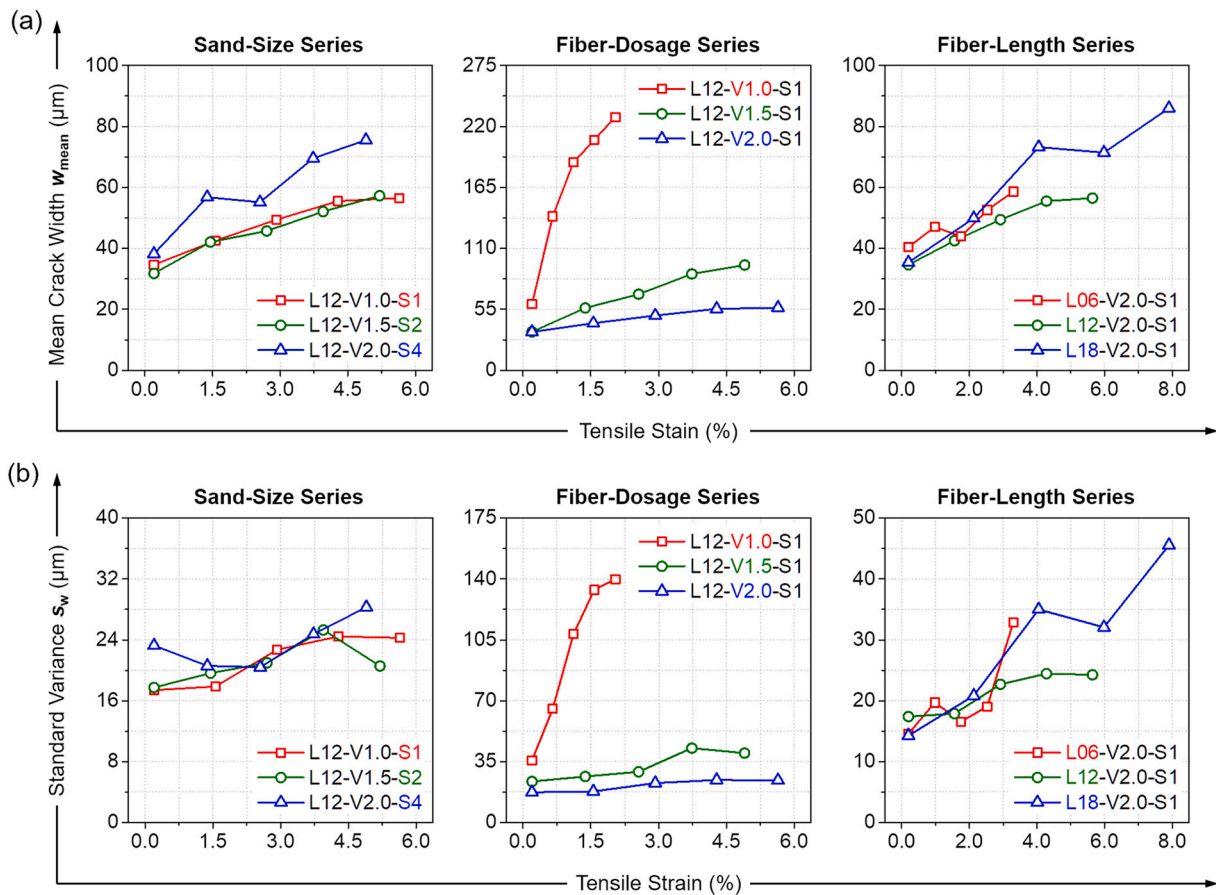


Fig. 7. (a) Mean values w_{mean} and (b) standard variances s_w of crack widths at different tensile strain levels. The values of w_{mean} and s_w increase as the tensile strain increases. Larger sand size and lower fiber dosage result in larger crack widths under the same tensile strain. Fiber length has no obvious effect under the same tensile strain below 2%.

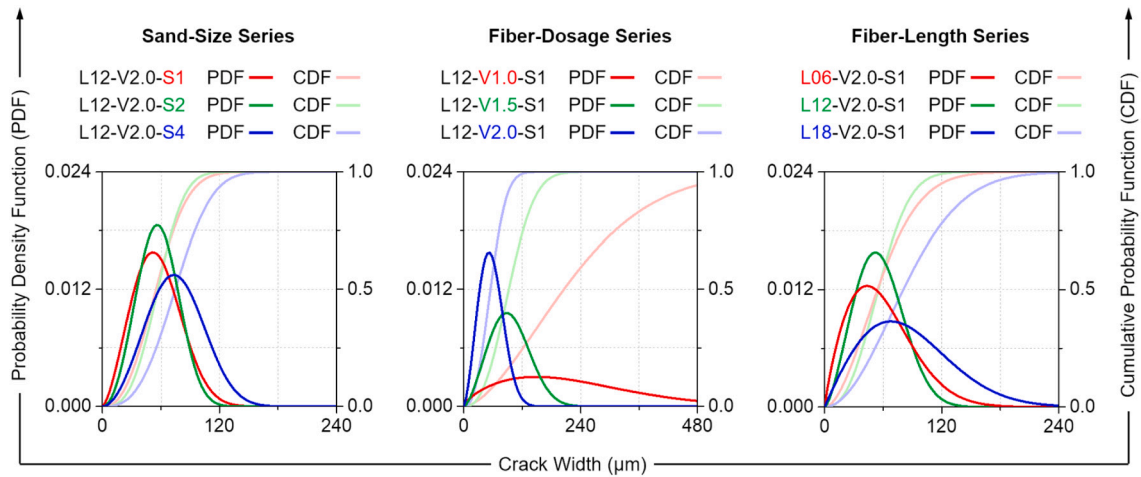


Fig. 8. Crack width distributions of SS-ECC at the ultimate stage (strain level E). Larger sand size, lower fiber dosage and larger fiber length (likely due to fiber rupture) result in larger crack widths at the ultimate stage.

Table 5
Inputs for micromechanical modeling of L12-V2.0-S1 and L18-V2.0-S1.

Micromechanical parameters		Values
Fiber parameters	Fiber length, L_f (mm)	12 or 18
	Fiber diameter, d_f (μm)	24
	Fiber elastic modulus, E_f (GPa)	120 ^a
	Fiber strength, σ_{fu} (MPa)	3000 ^a
	Interfacial chemical bond, G_d (J/m ²)	0 ^b
	Interfacial frictional bond, τ_0 (MPa)	1.68 ^c
Interface parameters	Frictional bond reduction factor, γ	0.67 ^d
	Slip-hardening coefficient, β	0.003 ^c
	Snubbing coefficient, f	0.59 ^e
	Fiber strength reduction factor, f'	0.33 ^d
	Cook-Gordon effect parameter, α	360 ^f
	Elastic modulus, E_m (MPa)	37 ^c
Matrix parameters	Fracture toughness, K_m (MPa·m ^{1/2})	0.611 ^c
	Cracking strength, σ_{fc} (MPa)	4.2 ^c
	Matrix-spalling parameter, k	200 ^g

^a Nominal properties from the fiber supplier (Table 2).
^b The chemical bond was assumed to be zero for PE fibers with hydrophobic surface.
^c Test results in this study;
^d These values were assumed according to Ref. [61];
^e This value was assumed according to Ref. [62];
^f $\alpha = 15d_f$ as suggested in Ref. [63];
^g This value was estimated according to the experimental observation on the size of spalling matrix and an empirical equation in Ref. [61].

4.3. Analysis of crack characteristics based on the Weibull distribution

For the Weibull distribution of crack width, the mean value (w_{mean}) and standard variance (s_w) of crack width are expressed as follows:

$$w_{mean} = \lambda \Gamma(1 + 1/k) \tag{5}$$

$$s_w = \lambda \sqrt{\Gamma(1 + 2/k) - (\Gamma(1 + 1/k))^2} \tag{6}$$

On the basis of Eq. (5) and Eq. (6), the mean values (w_{mean}) and standard variances (s_w) of crack widths at different tensile strain levels were calculated and plotted in Fig. 7a and Fig. 7b, respectively. The w_{mean} and s_w of different SS-ECC under the same tensile strain value can then be compared.

In general, the values of w_{mean} and s_w increased as the tensile strain increased. For the sand-size series, the w_{mean} and s_w of L12-V2.0-S1 and L12-V2.0-S2 were close to each other, while those of L12-V2.0-S4 were the largest. The maximum sand particle size of L12-V2.0-S4 (4.75 mm) was more than 1/3 of the thickness of the tensile specimen (13 mm). The large-size sand affected the uniform distribution of PE fibers, resulting in larger crack width of L12-V2.0-S4 in the sand-size series. For the fiber-dosage series, the w_{mean} and s_w decreased with the increase in fiber dosage, because of the expected increase in the fiber-bridging stress resisting the crack opening. For the fiber-length series, the w_{mean} and s_w of the three groups were very close to each other at the strain level below 2%, but their values for L18-V2.0-S1 are larger than those of L06-V2.0-

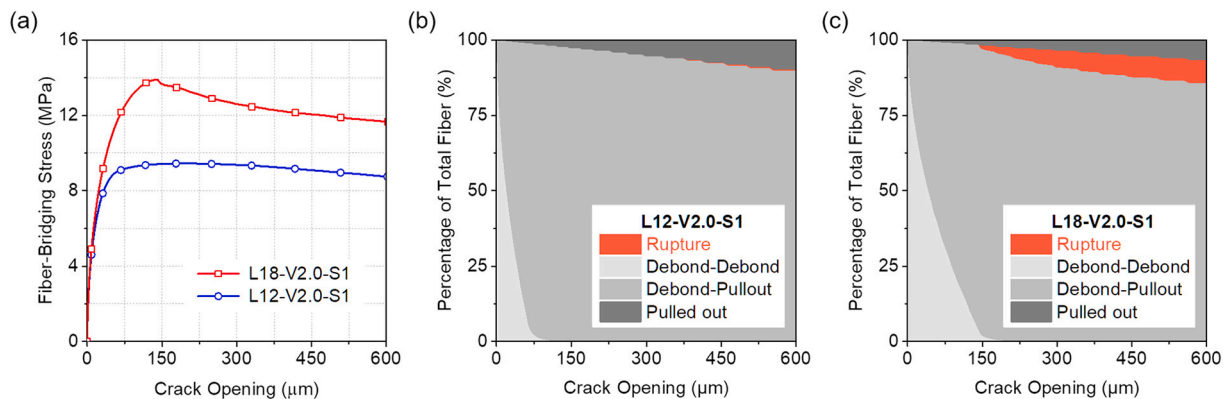


Fig. 9. Results of micromechanical modeling [41]: (a) fiber-bridging stress vs. crack opening, (b) fiber status of L12-V2.0-S1, and (c) fiber status of L18-V2.0-S1. The fiber-bridging stress is higher in SS-ECC with longer fibers at the same crack opening. A significant fraction of ruptured fibers can be found in the 18-mm case when the crack opening is larger than 150 μm, while almost no fiber rupture is found in the 12-mm case.

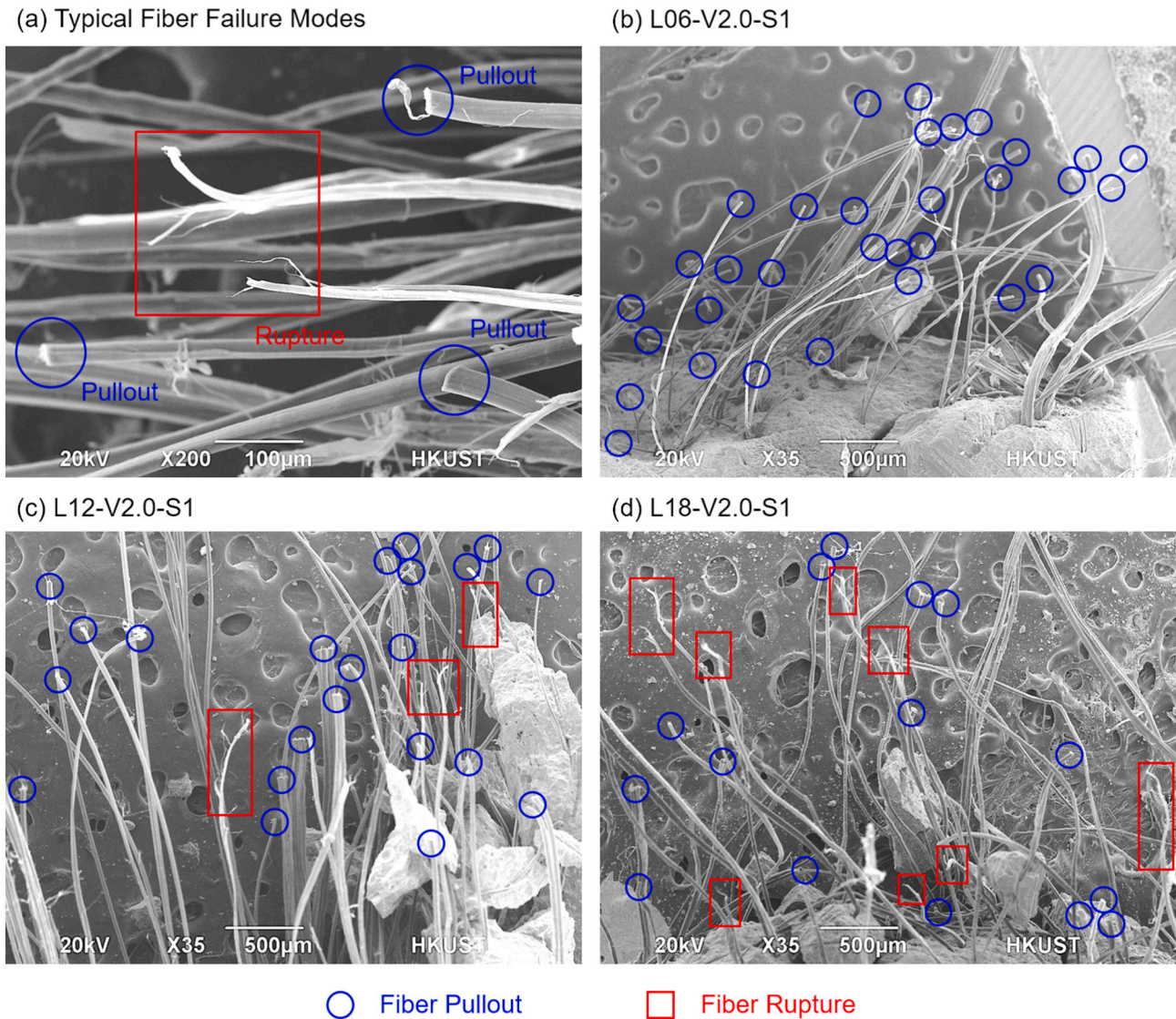


Fig. 10. SEM images for the PE fiber status at the final failure crack under tension: (a) typical fiber failure modes, (b) L06-V2.0-S1, (c) L12-V2.0-S1, and (d) L18-V2.0-S1. With increasing fiber length, the fraction of rupture fibers increases.

S1 and L12-V2.0-S1 at higher strain values. With longer embedment length, the fibers in L18-V2.0-S1 are more likely to rupture at a larger crack opening during the tensile strain-hardening process. This phenomenon is further analyzed based on micromechanical modeling and SEM observation in the next section.

Specifically, the crack width distributions (both PDF and CDF) of SS-ECC at the ultimate stage (strain level E) are presented in Fig. 8. The results were similar to those presented in Fig. 7: larger sand size, lower fiber dosage and larger fiber length (likely due to fiber rupture) resulted in larger crack widths at the ultimate stage.

4.4. Micromechanical and SEM analysis on fiber status

To theoretically investigate the fiber status in SS-ECC, the micromechanical analysis was carried out for L12-V2.0-S1 and L18-V2.0-S1 using an updated model reported in Yang et al. [61]. Table 5 presents the matrix, fiber, and interface parameters used in the modeling, while more details on these parameters can be found in Yang et al. [61]. It should be noted that a random two-dimensional fiber distribution was assumed, because the SS-ECC was cast into a 13-mm thick mold in two equal layers and the fiber length (12 mm) was larger than the thickness of each layer. The modeled results are shown in Fig. 9, including the

fiber-bridging stress vs. crack-opening relationship (Fig. 9a) and the fiber statuses (Fig. 9b-c). For the fiber status, “Rupture” means the carried stress exceeds the fiber strength; “Debond-Debond” means both sides of the fiber are undergoing debonding; “Debond-Pullout” means the short side of the fiber is being pull-out and the long side is undergoing debonding; and “Pulled out” means the short side of fiber is completely pulled out from the matrix.

As shown in Fig. 9a, the fiber-bridging stress is higher in SS-ECC with longer fibers at the same crack opening. With increasing fiber length, the average embedded length of fibers in the matrix increases, and it leads to a larger interfacial frictional force acting on the fiber. The higher interfacial frictional force on the 18-mm fibers results in a higher percentage of ruptured fibers when the crack opening is large enough (Fig. 9c). The fiber rupture led to lower crack-bridging capacity and larger crack width in L18-V2.0-S1 after a certain crack opening (as well as a certain strain level), which is consistent with the observations in Figs. 7 and 8.

The fiber status at the final failure crack under tension was experimentally verified by the SEM analysis (Fig. 10). Two typical fiber failure modes (i.e., pullout and rupture) can be observed at the final failure crack (Fig. 10a). The SEM images of L06-V2.0-S1, L12-V2.0-S1, and L18-V2.0-S1 with the same magnification are presented in Fig. 10b, c, and d,

Table 6

Mean values (w_{mean}) and standard variances (s_w) of the crack widths at the ultimate stage (strain level E) for the selected samples.

Specimen ID	w_{mean} (μm)	$1/w_{\text{mean}}$ ($1/\mu\text{m}$)	s_w (μm)	$1/s_w$ ($1/\mu\text{m}$)
L12-V2.0-S1	56.5	0.018	24.3	0.041
L12-V2.0-S2	57.3	0.017	20.6	0.049
L12-V2.0-S4	75.5	0.013	28.3	0.035
L12-V1.0-S1	228.4	0.004	139.8	0.007
L12-V1.5-S1	95.0	0.011	39.9	0.025
L06-V2.0-S1	58.6	0.017	32.9	0.030
L18-V2.0-S1	86.0	0.012	45.6	0.022

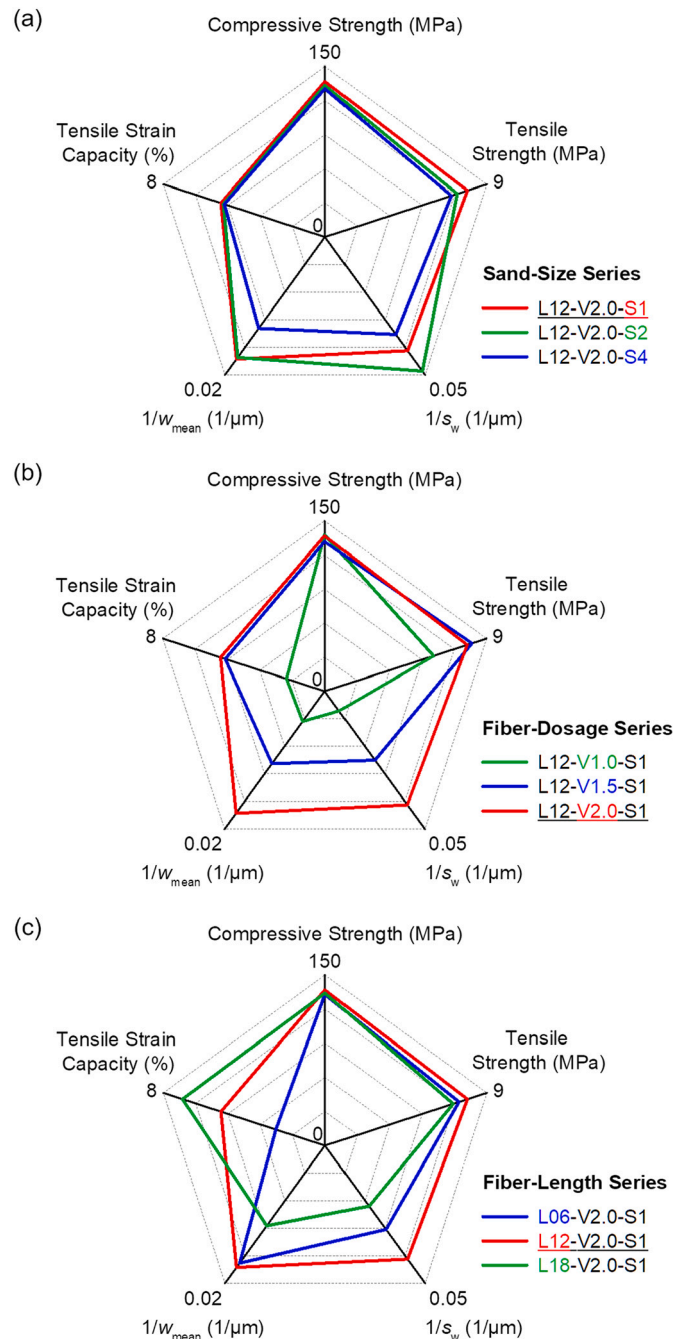


Fig. 11. Five-dimensional assessment considering both mechanical and cracking performance of SS-ECC using radar graph. The overall performance of L12-V2.0-S1 and L12-V2.0-S2 is outstanding among all the SS-ECC mixes studied.

respectively. It can be found that almost all the fibers of L06-V2.0-S1 are pulled out (Fig. 10b), while both pullout and rupture failure modes can be observed for L12-V2.0-S1 (Fig. 10c) and L18-V2.0-S1 (Fig. 10d). Overall, with increasing fiber length, the fraction of ruptured fibers increases. These observations coincide with the micromechanical modeling results (Fig. 9).

4.5. Overall assessment of SS-ECC by considering both mechanical and cracking performance

For a ECC structural component, the compressive and tensile strength as well as the tensile strain capacity are the key mechanical performance indices, while the crack width and variance are critical for its mechanical and durability performance. Specifically, small crack width can also improve the deformation compatibility between ECC and FRP reinforcement. Therefore, the smaller w_{mean} and s_w the better: the smaller w_{mean} is beneficial to the water permeability and self-healing performance, and the smaller s_w means the multiple-cracking behavior is more stable.

Based on Eq. (5) and Eq. (6), the mean values (w_{mean}) and standard variances (s_w) of crack widths at the ultimate stage (strain level E) for the selected samples are calculated and listed in Table 6. To obtain the positive relations between the assessment indices and crack characteristics, the reciprocals of w_{mean} and s_w (i.e., $1/w_{\text{mean}}$ and $1/s_w$ in Table 6) can be used to assess the cracking performance of SS-ECC.

To assess the overall performance of SS-ECC, a five-dimensional representation of the cracking performance (i.e., crack width and its variation) and the mechanical performance (i.e., compressive and tensile properties) is proposed (Fig. 11). The effects of the sand size, fiber dosage, and fiber length on the overall performance are presented in Fig. 11a, b and c, respectively. For the sand-size series, the overall performance of L12-V2.0-S1 and L12-V2.0-S2 were close to each other in general, and L12-V2.0-S4 showed poorer cracking performance. For the fiber-dosage series, the overall performance of SS-ECC (except compressive strength) significantly improved as the fiber dosage increased. For the fiber-length series, the tensile strain capacity of L18-V2.0-S1 was the highest, but its crack-control capacity was the lowest.

Based on the above discussion, the overall performance of L12-V2.0-S1 and L12-V2.0-S2 is outstanding among all the SS-ECC mixes studied. Additionally, from the perspective of the utilization rate of raw material (Table 3), sea-sand is more effectively used in L12-V2.0-S2 as compared to L12-V2.0-S1. In summary, L12-V2.0-S2 is highly recommended for practical marine and coastal applications.

5. Probabilistic modeling of crack width evolution with increasing tensile strain

In this section, a probabilistic model is developed to describe the crack width evolution of SS-ECC at different strain levels. First, the functions linking the Weibull scale and shape parameters to the tensile strain levels are introduced. Second, the probabilistic model is developed and validated by comparing the model results with the test data of L12-V2.0-S1 and L12-V2.0-S2 that showed the best overall performance. Finally, a possible application of the proposed model is presented.

5.1. Weibull scale and shape parameters vs. tensile strain

5.1.1. Weibull scale parameter

Based on the results in Table 4, the Weibull scale parameter λ vs. tensile strain ϵ relations of SS-ECC are presented in Fig. 12, and the tensile stress-strain curves are also plotted for comparison. Generally, the Weibull scale parameter λ increased with increasing tensile strain ϵ . It can be observed that the λ - ϵ relations coincide with the strain-hardening branches of the stress-strain curves. This phenomenon can be explained as follows. The crack width of SS-ECC increased as the tensile strain increased (Fig. 7a). For the λ - ϵ relations, the value of λ and

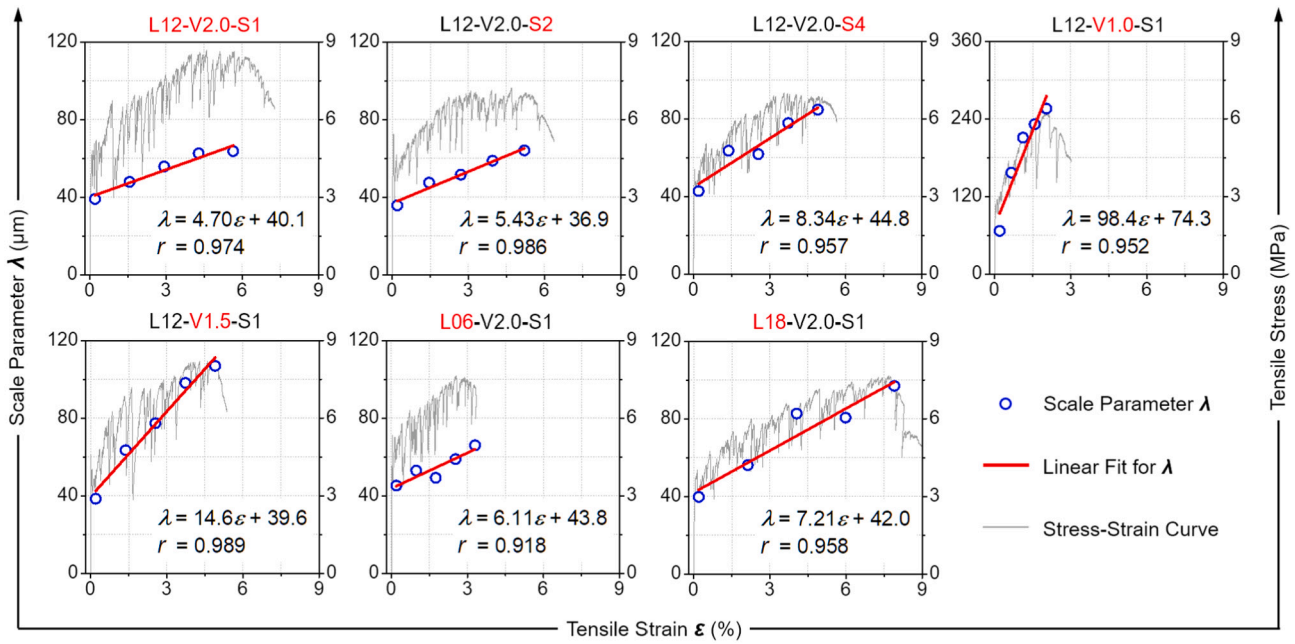


Fig. 12. Weibull scale parameter (λ) of crack widths at different tensile strain levels for the selected SS-ECC samples. A linear relationship is observed between the Weibull scale parameter λ and the tensile strain ϵ .

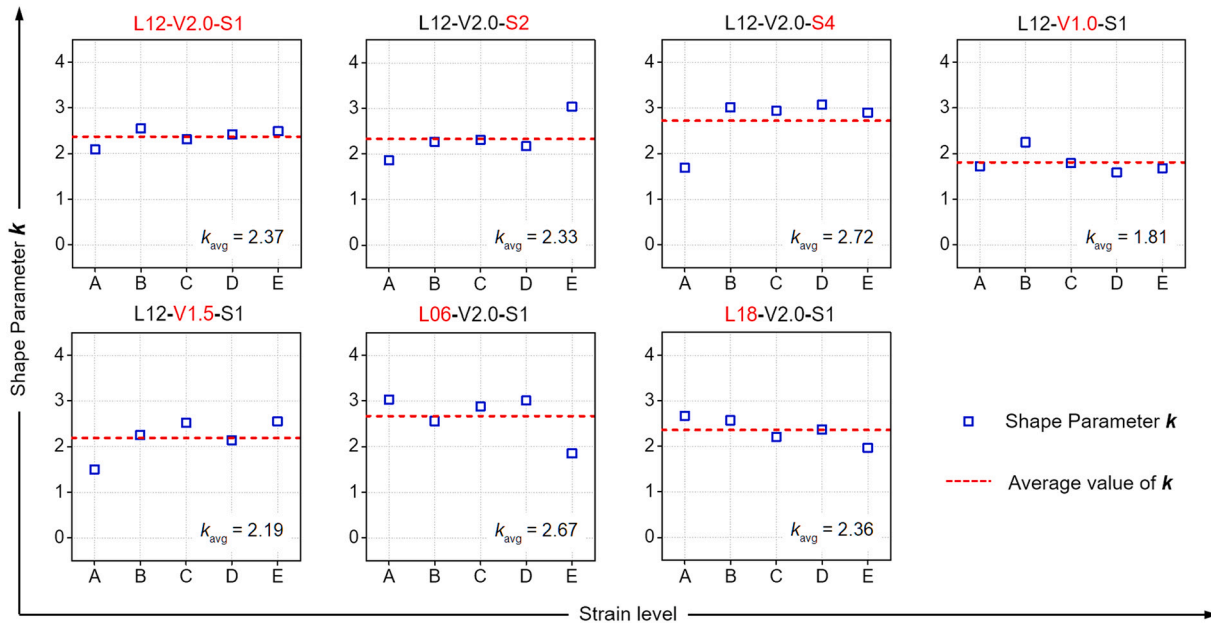


Fig. 13. Weibull shape parameter (k) of crack widths at different tensile strain levels for the selected SS-ECC samples. The variation of the k values at different strain levels is marginal.

crack width have a positive correlation [Eq. (5)]. For the stress-strain curves, the fiber bridging stress (before the peak stress) increased with increasing crack width (Fig. 9a). Thus, the trends of λ - ϵ relations and stress-strain curves (Fig. 12) are similar. When linear fit was applied to describe the λ - ϵ relation for each selected sample, the correlation coefficient r ranged from 0.918 to 0.989, which indicates a strong linear correlation between λ and ϵ . Therefore, the following simplified linear relation (Eq. (7)) between λ and ϵ can be used for further discussion:

$$\lambda = A\epsilon + B \quad (7)$$

where A and B are the coefficients from the linear fitting.

5.2. Weibull shape parameter

Based on the results in Table 4, the Weibull shape parameter k vs. tensile strain ϵ relations of SS-ECC are presented in Fig. 13, and the average value of k (i.e., k_{avg}) for each selected sample is also plotted with a dashed line. The variation of the k values at different strain levels is limited in general, except for a few data points. Hence, for simplicity, the Weibull shape parameter k is assumed to be a constant (i.e., the average value k_{avg}) for each group in the probabilistic modeling (Eq. (8)). The applicability of this simplification will be discussed later.

$$k = k_{avg} \quad (8)$$

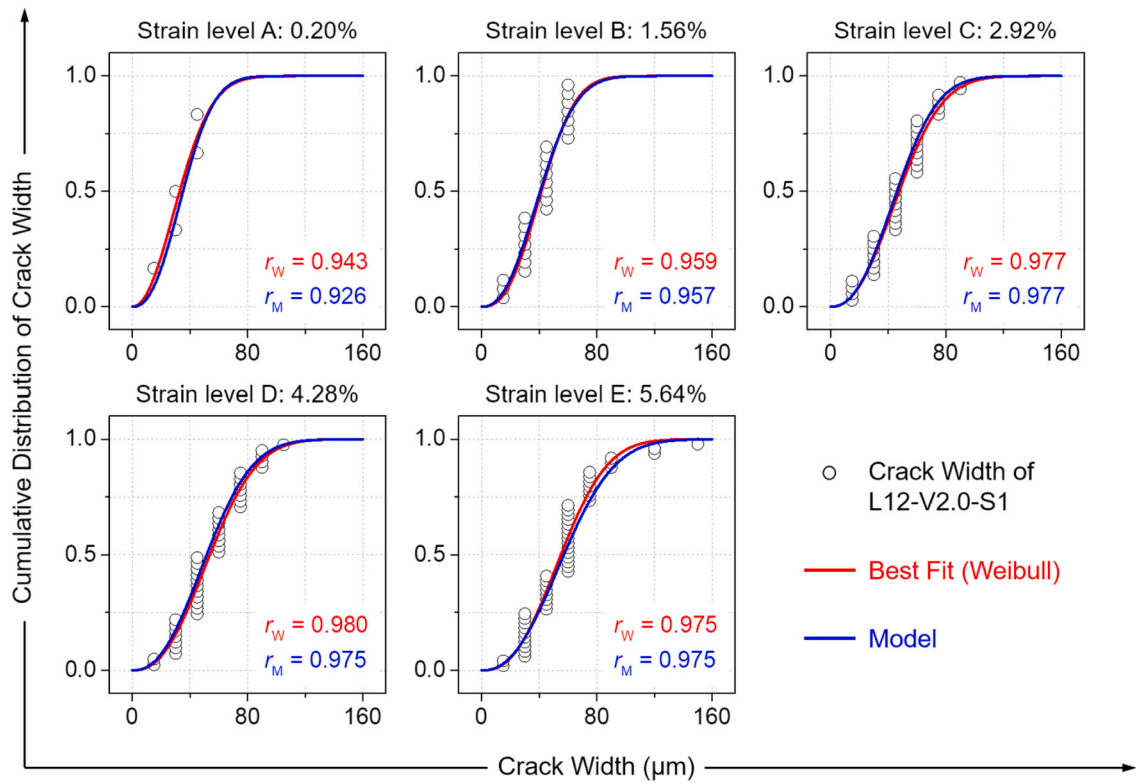


Fig. 14. Modeling results of the cumulative distribution of crack widths for L12-V2.0-S1 show good agreement with test results.

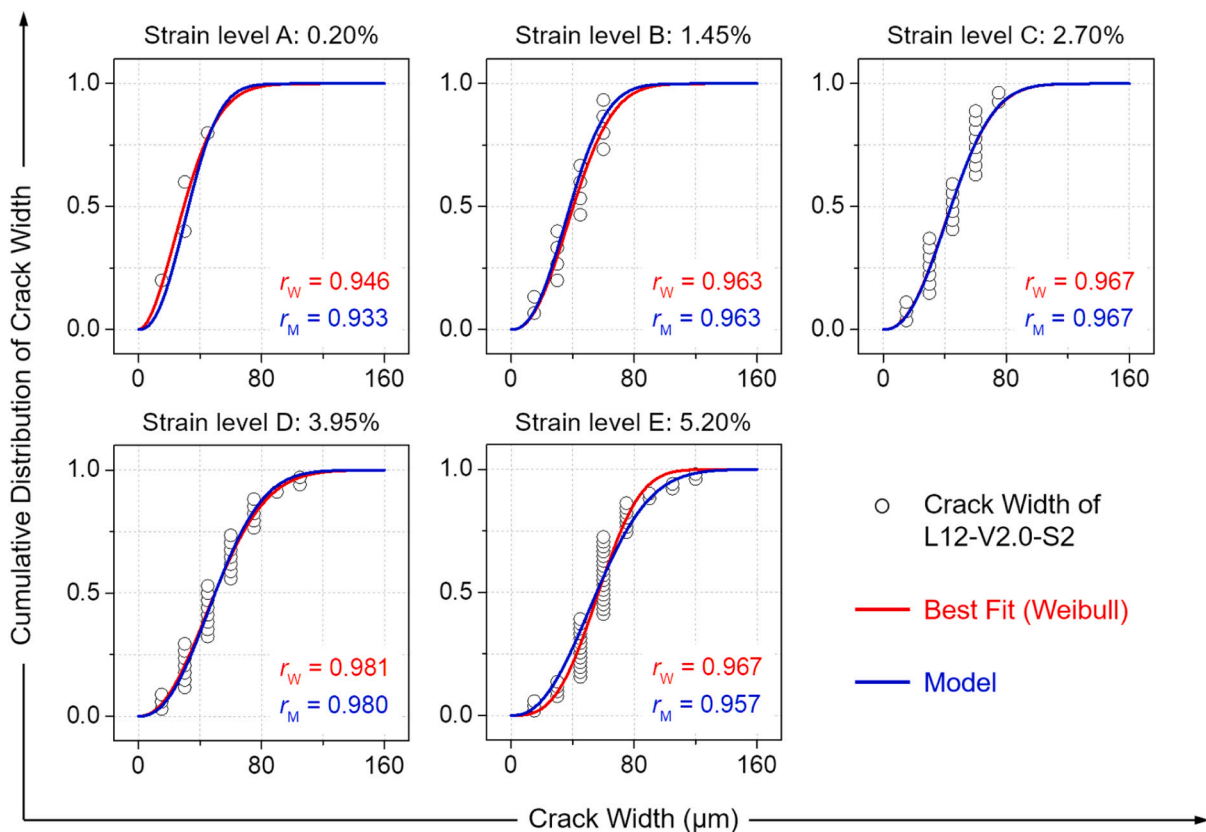


Fig. 15. Modeling results of the cumulative distribution of crack widths for L12-V2.0-S2 show good agreement with test results.

5.3. Probabilistic modeling and validation

By introducing Eq. (7) and Eq. (8) into the Weibull cumulative distribution function (CDF, Eq. (4)), the CDF of crack width w at a given tensile strain ε can be expressed as:

$$F(w) = 1 - \exp\left(-\left(\frac{w}{A\varepsilon + B}\right)^{k_{avg}}\right) \quad (9)$$

where the determinations of A , B , and k_{avg} are shown in Figs. 12 and 13. To validate the applicability of the model, the modeling result at every strain level (from A to E) was compared to the experimental and best-fit results. Figs. 14 and 15 presents the detail of the comparison for L12-V2.0-S1 and L12-V2.0-S2, respectively. It should be pointed out that the best-fit result was directly fitted from the measured crack widths (from experiment) using the Weibull distribution. In the figures, r_W and r_M are the correlation coefficients of the best-fit and modeling cumulative distribution curves, respectively. In general, the values of r_M were very close to those of r_W , which indicates that the modeling results are very close to the best-fit ones. Additionally, it validates the treating of the Weibull shape parameter k as a constant [i.e., Eq. (8)] at all the strain levels.

According to Eq. (9), the crack width w for a given tensile strain ε and cumulative probability $F(w)$ can be derived as follows:

$$w = (A\varepsilon + B)(-\ln(1 - F(w)))^{1/k_{avg}} \quad (10)$$

The modeling and test results of the probability densities of the crack widths at different strain levels for L12-V2.0-S1 and L12-V2.0-S2 are plotted in Figs. 16 and 17, respectively. Additionally, the crack width vs. tensile strain relation at three different cumulative probabilities (i.e., 0%, 50% and 99%) are also presented in Figs. 16 and 17 for demonstration. In general, the modeling results showed good agreement with the test results, which indicates that this method can satisfactorily model the crack width evolution of SS-ECC. It should be pointed out that the proposed method can also satisfactorily model the crack width evolution of other SS-ECC mixes in this study, but the corresponding results are not particularly presented in this section.

5.4. Demonstration of the application of the model

It is known that the crack width is critical for the water permeability and self-healing behavior of concrete materials [3]. To control the crack width of SS-ECC in practical applications, the proposed model can be

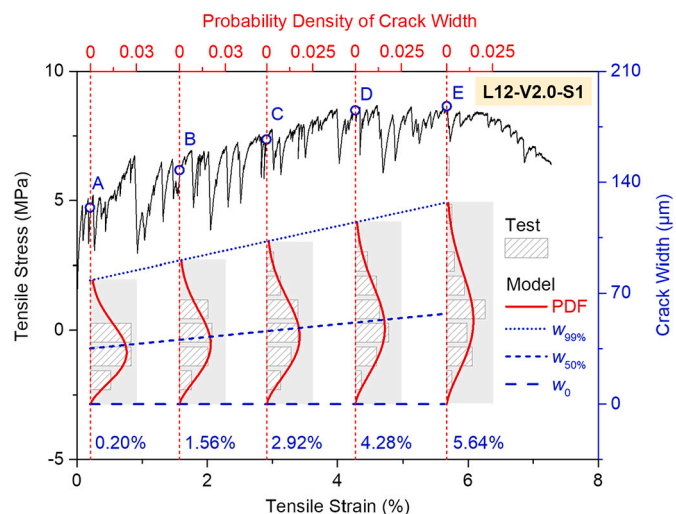


Fig. 16. Modeling results of the crack width distributions of L12-V2.0-S1 at different strain levels show good agreement with test results.

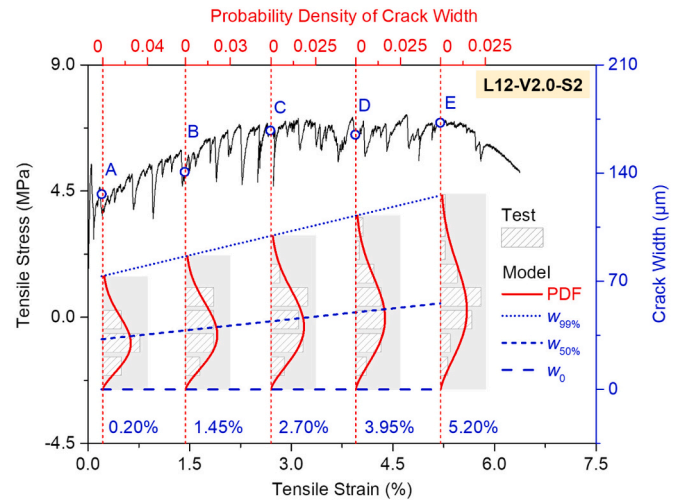


Fig. 17. Modeling results of the crack width distributions of L12-V2.0-S2 at different strain levels show good agreement with test results.

used to estimate the critical tensile strain for a given crack width limit and cumulative probability by using Eq. (11).

$$\varepsilon = \frac{w/A}{(-\ln(1 - F(w)))^{1/k_{avg}}} - \frac{B}{A} \quad (11)$$

For all the selected samples in Fig. 4, the critical tensile strain vs. crack width limit relations are plotted in Fig. 18. It should be pointed out that the crack width limit $w_{99\%}$ means that 99% of the cracks are controlled to have the width below this value.

For ECC materials, the crack with the width no more than 100 μm are likely to have excellent self-healing performance [42]. Compared to the other groups, L12-V2.0-S1 and L12-V2.0-S2 have the largest critical tensile strains for the same crack width limit, as L12-V2.0-S1 and L12-V2.0-S2 have the best crack-control capacity among the SS-ECC mixes studied (Fig. 11). By introducing $F(w) = 99\%$ and $w_{99\%} = 100 \mu\text{m}$ into Eq. (11), the critical tensile strains on L12-V2.0-S1 or L12-V2.0-S2 can be estimated to be no more than 2.64% and 2.77%, respectively.

6. Conclusions

This study assesses the crack characteristics and models the crack width evolution in high-strength seawater sea-sand Engineered Cementitious Composites (SS-ECC), considering the effects of ingredient parameters including sand size (1.18 mm, 2.36 mm and 4.75 mm), fiber length (6 mm, 12 mm, and 18 mm), and fiber volume dosage (1.0%, 1.5%, and 2.0% for 12-mm fibers). Based on the materials used and results obtained, the following conclusions can be made.

- 1) According to the experimental observation, micromechanical modeling and SEM analysis, smaller sand size and higher fiber dosage of SS-ECC resulted in smaller crack widths under the same tensile strain. Fiber length had no obvious effect under the same tensile strain below 2%, but 18-mm fiber led to larger crack widths at a strain level above 2%, due to a large fraction of fiber rupture after a certain crack opening.
- 2) For SS-ECC with 1.0–2.0 vol% fibers, the Weibull distribution was found to describe the crack width distribution better than the log-normal distribution, at all tensile strain levels.
- 3) A five-dimensional representation of crack characteristics and mechanical performance was introduced to graphically assess the overall performance of SS-ECC. According to this assessment, the overall performance of L12-V2.0-S1 and L12-V2.0-S2 was outstanding among all the SS-ECC mixes studied. Additionally,

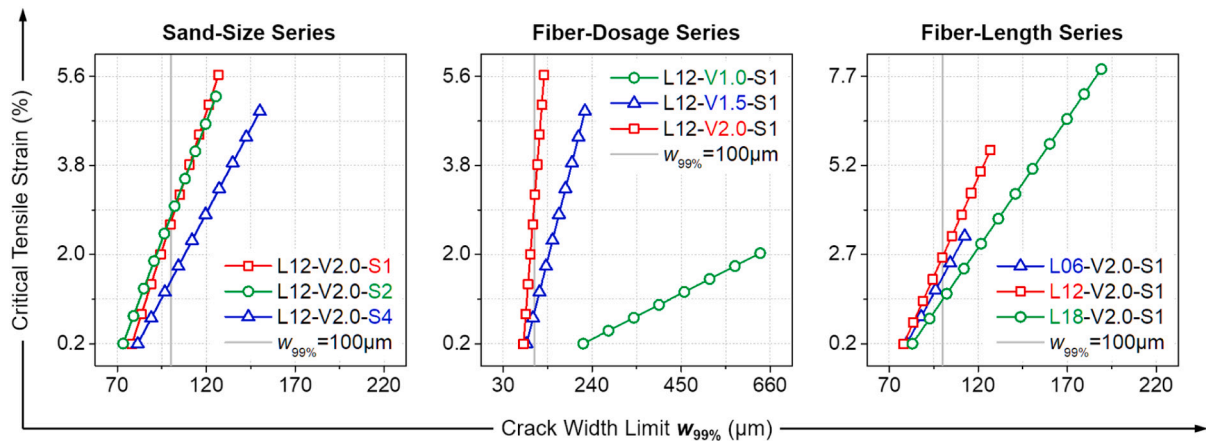


Fig. 18. Critical tensile strain vs. crack width limit relations of SS-ECC. For the same crack width limit, the critical tensile strains of L12-V2.0-S1 and L12-V2.0-S2 are the largest.

considering the utilization rate of raw material (sea-sand), L12-V2.0-S2 is highly recommended for practical applications.

- 4) A probabilistic approach was proposed to model the stochastic nature and evolution of the crack width distributions of SS-ECC at different strain levels. The modeling results showed good agreement with the experimental results, and it can be used to estimate the critical tensile strain on SS-ECC in practical applications for a given crack width limit and cumulative probability. Specifically, if the crack widths of SS-ECC need to be controlled to no more than 100 μm for 99% of the cracks, the applied tensile strains for L12-V2.0-S1 and L12-V2.0-S2 should be no more than 2.64% and 2.77%, respectively.

The above findings and proposed methods can facilitate the future application of SS-ECC in marine and coastal structures. It should be pointed out that the proposed assessment method by comprehensively considering the mechanical performance and crack characteristics can also be used in other kinds of strain-hardening cement-based materials. Additionally, as the proposed probabilistic modeling method was only demonstrated to be effective for SS-ECC in this study, its applicability for conventional ECC should be further verified.

CRedit authorship contribution statement

Bo-Tao Huang: Conceptualization, Methodology, Investigation, Visualization, Writing - original draft. **Jia-Qi Wu:** Investigation, Validation. **Jing Yu:** Conceptualization, Methodology, Investigation, Data curation, Writing - review & editing. **Jian-Guo Dai:** Conceptualization, Funding acquisition, Supervision. **Christopher K.Y. Leung:** Funding acquisition, Supervision. **Victor C. Li** Supervision, Writing - review & editing.

Declaration of competing interest

The authors declare that they have no known competing financial interests or personal relationships that could have appeared to influence the work reported in this paper.

Acknowledgments

This study was supported by the Innovation Technology Fund of the Hong Kong Government (No. ITS/077/18FX) and the Hong Kong Research Grants Council (No. T22-502/18-R). Bo-Tao Huang acknowledges the support by The Hong Kong Polytechnic University through the Research Institute for Sustainable Urban Development (No. 1-BBWE) and the Postdoctoral Fellowships Scheme (No. YW4K). The authors would also thank Mr. Yu-Tian Wang for his help in the analysis of crack

characteristics, and Dr. Yu Xiang, Mr. Ke-Fan Weng and Mr. Ji-Xiang Zhu for their assistance in experimental work.

References

- [1] V.C. Li, C.K.Y. Leung, Steady-state and multiple cracking of short random fiber composites, *J. Eng. Mech.* 118 (11) (1992) 2246–2264.
- [2] C.K.Y. Leung, Design criteria for pseudoductile fiber-reinforced composites, *J. Eng. Mech.* 122 (1) (1996) 10–18.
- [3] V.C. Li, *Engineered Cementitious Composites (ECC) - Bendable Concrete for Sustainable and Resilient Infrastructure*, Springer, Berlin, Heidelberg, Verlag GmbH Germany, 2019.
- [4] D. Zhang, J. Yu, H. Wu, B. Jaworska, B.R. Ellis, V.C. Li, Discontinuous Micro-Fibers as Intrinsic Reinforcement for Ductile Engineered Cementitious Composites (ECC), *Engineering, Composites Part B*, 2020, p. 107741.
- [5] J. Yu, J. Yao, X. Lin, H. Li, J.Y. Lam, C.K.Y. Leung, I.M.L. Sham, K. Shih, Tensile performance of sustainable strain-hardening cementitious composites with hybrid PVA and recycled PET fibers, *Cem. Concr. Res.* 107 (2018) 110–123.
- [6] X. Lin, J. Yu, H. Li, J.Y.K. Lam, K. Shih, I.M.L. Sham, C.K.Y. Leung, Recycling polyethylene terephthalate wastes as short fibers in strain-hardening cementitious composites (SHCC), *J. Hazard. Mater.* 357 (2018) 40–52.
- [7] B.T. Huang, Q.H. Li, S.L. Xu, L. Zhang, Static and fatigue performance of reinforced concrete beam strengthened with strain-hardening fiber-reinforced cementitious composite, *Eng. Struct.* 199 (2019) 109576.
- [8] Q.H. Li, B.T. Huang, S.L. Xu, Development of assembled permanent formwork using ultra high toughness cementitious composites, *Adv. Struct. Eng.* 19 (7) (2016) 1142–1152.
- [9] B.T. Huang, Q.H. Li, S.L. Xu, B.M. Zhou, Frequency effect on the compressive fatigue behavior of ultrahigh toughness cementitious composites: experimental study and probabilistic analysis, *J. Struct. Eng.* 143 (8) (2017), 04017073.
- [10] B.T. Huang, Q.H. Li, S.L. Xu, W. Liu, H.T. Wang, Fatigue deformation behavior and fiber failure mechanism of ultra-high toughness cementitious composites in compression, *Mater. Des.* 157 (2018) 457–468.
- [11] K.Q. Yu, J.T. Yu, J.G. Dai, Z.D. Lu, S.P. Shah, Development of ultra-high performance engineered cementitious composites using polyethylene (PE) fibers, *Constr. Build. Mater.* 158 (2018) 217–227.
- [12] J. Yu, H.-L. Wu, C.K.Y. Leung, Feasibility of using ultrahigh-volume limestone-calcined clay blend to develop sustainable medium-strength engineered cementitious composites (ECC), *J. Clean. Prod.* 262 (2020) 121343.
- [13] Y. Alrefaie, J.-G. Dai, Tensile behavior and microstructure of hybrid fiber ambient cured one-part engineered geopolymer composites, *Constr. Build. Mater.* 184 (2018) 419–431.
- [14] J. Yu, Y. Chen, C.K. Leung, Mechanical performance of strain-hardening cementitious composites (SHCC) with hybrid polyvinyl alcohol and steel fibers, *Compos. Struct.* 226 (2019) 111198.
- [15] P. Jun, V. Mechtcherine, Behaviour of strain-hardening cement-based composites (SHCC) under monotonic and cyclic tensile loading: part 1—experimental investigations, *Cem. Concr. Compos.* 32 (10) (2010) 801–809.
- [16] B.T. Huang, Q.H. Li, S.L. Xu, B.M. Zhou, Tensile fatigue behavior of fiber-reinforced cementitious material with high ductility: experimental study and novel P-S-N model, *Constr. Build. Mater.* 178 (2018) 349–359.
- [17] B.T. Huang, Q.H. Li, S.L. Xu, Fatigue deformation model of plain and fiber-reinforced concrete based on Weibull function, *J. Struct. Eng.* 145 (1) (2019), 04018234.
- [18] V. Mechtcherine, O. Millon, M. Butler, K. Thoma, Mechanical behaviour of strain hardening cement-based composites under impact loading, *Cem. Concr. Compos.* 33 (1) (2011) 1–11.

- [19] C. Lu, J. Yu, C.K.Y. Leung, Tensile performance and impact resistance of strain hardening cementitious composites (SHCC) with recycled fibers, *Constr. Build. Mater.* 171 (2018) 566–576.
- [20] Y.Y. Kim, H.J. Kong, V.C. Li, Design of engineered cementitious composite suitable for wet-mixture shotcreting, *ACI Mater. J.* 100 (6) (2003) 511–518.
- [21] B.T. Huang, Q.H. Li, S.L. Xu, B. Zhou, Strengthening of reinforced concrete structure using sprayable fiber-reinforced cementitious composites with high ductility, *Compos. Struct.* 220 (2019) 940–952.
- [22] C.K. Leung, Q. Cao, Development of pseudo-ductile permanent formwork for durable concrete structures, *Mater. Struct.* 43 (7) (2010) 993–1007.
- [23] B.T. Huang, Q.H. Li, S.L. Xu, C.F. Li, Development of reinforced ultra-high toughness cementitious composite permanent formwork: experimental study and digital image correlation analysis, *Compos. Struct.* 180 (2017) 892–903.
- [24] V.C. Li, F.P. Bos, K. Yu, W. McGee, T.Y. Ng, S.C. Figueiredo, K. Nefs, V. Mechtcherine, V.N. Nerella, J. Pan, G.P. van Zijl, P.J. Kruger, On the emergence of 3D printable engineered, strain hardening cementitious composites (ECC/SHCC), *Cem. Concr. Res.* 132 (2020) 106038.
- [25] B. Zhu, J. Pan, B. Nematollahi, Z. Zhou, Y. Zhang, J. Sanjayan, Development of 3D printable engineered cementitious composites with ultra-high tensile ductility for digital construction, *Mater. Des.* 181 (2019) 108088.
- [26] J. Xiao, C. Qiang, A. Nanni, K. Zhang, Use of sea-sand and seawater in concrete construction: current status and future opportunities, *Constr. Build. Mater.* 155 (2017) 1101–1111.
- [27] J.G. Teng, Y. Xiang, T. Yu, et al., Development and mechanical behaviour of ultra-high-performance seawater sea-sand concrete, *Adv. Struct. Eng.* 22 (14) (2019) 3100–3120.
- [28] A. Ahmed, S. Guo, Z. Zhang, C. Shi, D. Zhu, A review on durability of fiber reinforced polymer (FRP) bars reinforced seawater sea sand concrete, *Constr. Build. Mater.* 256 (2020) 119484.
- [29] Y.L. Li, X.L. Zhao, R.S. Raman, X. Yu, Axial compression tests on seawater and sea sand concrete-filled double-skin stainless steel circular tubes, *Eng. Struct.* 176 (2018) 426–438.
- [30] Z. Dong, G. Wu, X.L. Zhao, H. Zhu, J.L. Lian, The durability of seawater sea-sand concrete beams reinforced with metal bars or non-metal bars in the ocean environment, *Adv. Struct. Eng.* 23 (2) (2020) 334–347.
- [31] A. Dasar, D. Patah, H. Hamada, Y. Sagawa, D. Yamamoto, Applicability of seawater as a mixing and curing agent in 4-year-old concrete, *Constr. Build. Mater.* 259 (2020) 119692.
- [32] G. Wu, Z.S. Wu, Y.B. Luo, Z.Y. Sun, X.Q. Hu, Mechanical properties of steel-FRP composite bar under uniaxial and cyclic tensile loads, *J. Mater. Civ. Eng.* 22 (10) (2010) 1056–1066.
- [33] Z. Dong, G. Wu, Y. Xu, Experimental study on the bond durability between steel-FRP composite bars (SFCBs) and sea sand concrete in ocean environment, *Constr. Build. Mater.* 115 (2016) 277–284.
- [34] Kang, S-B, Tan, K H, & Yang, E-H. (2015). Progressive collapse resistance of precast beam-column sub-assemblages with engineered cementitious composites. *Eng. Struct.*, 98(0), 186–200.
- [35] Yuan, F, Pan, J, Xu, Z, & Leung, C. K. Y. (2013). A comparison of engineered cementitious composites versus normal concrete in beam-column joints under reversed cyclic loading. *Mater. Struct.*, 46(1), 145–159.
- [36] Maalej, M, Ahmed, S. F. U., & Paramasivam, P. (2003). Corrosion durability and structural response of functionally-graded concrete beams. *J. Adv. Concr. Technol.*, 1(3), 307–316.
- [37] C.K.Y. Leung, Y.N. Cheung, J. Zhang, Fatigue enhancement of concrete beam with ECC layer, *Cem. Concr. Res.* 37 (5) (2007) 743–750.
- [38] G. Fischer, V.C. Li, Deformation behavior of fiber-reinforced polymer reinforced engineered cementitious composite (ECC) flexural members under reversed cyclic loading conditions, *ACI Struct. J.* 100 (1) (2003) 25–35.
- [39] M. Maalej, K.S. Leong, Engineered cementitious composites for effective FRP-strengthening of RC beams, *Compos. Sci. Technol.* 65 (7–8) (2005) 1120–1128.
- [40] B.T. Huang, J. Yu, J.Q. Wu, J.G. Dai, C.K.Y. Leung, Seawater sea-sand engineered cementitious composites (SS-ECC) for marine and coastal applications, *Composites Communications.* 20 (2020) 100353.
- [41] B.T. Huang, J.Q. Wu, J. Yu, J.G. Dai, C.K.Y. Leung, High-strength seawater sea-sand engineered cementitious composites (SS-ECC): mechanical performance and probabilistic modeling, *Cem. Concr. Compos.* 114 (2020) 103740.
- [42] Y. Yang, M.D. Lepech, E.H. Yang, V.C. Li, Autogenous healing of engineered cementitious composites under wet-dry cycles, *Cem. Concr. Res.* 39 (5) (2009) 382–390.
- [43] J. Qiu, S. Ruan, C. Unluer, E.-H. Yang, Autogenous healing of fiber-reinforced reactive magnesia-based tensile strain-hardening composites, *Cem. Concr. Res.* 115 (2019) 401–413.
- [44] H. Ma, E. Herbert, M. Ohno, V.C. Li, Scale-linking model of self-healing and stiffness recovery in engineered cementitious composites (ECC), *Cem. Concr. Compos.* 95 (2019) 1–9.
- [45] Z. Zhang, Q. Zhang, V.C. Li, Multiple-scale investigations on self-healing induced mechanical property recovery of ECC, *Cem. Concr. Compos.* 103 (2019) 293–302.
- [46] G.P. Van Zijl, V. Slowik (Eds.), *A Framework for Durability Design with Strain-hardening Cement-based Composites (SHCC): State-Of-The-Art Report of the RILEM Technical Committee 240-FDS*, Springer. Vol. 22 (2017).
- [47] M.D. Lepech, V.C. Li, Water permeability of engineered cementitious composites, *Cem. Concr. Compos.* 31 (10) (2009) 744–753.
- [48] C. Wagner, B. Villmann, V. Slowik, V. Mechtcherine, Water permeability of cracked strain-hardening cement-based composites, *Cem. Concr. Compos.* 82 (2017) 234–241.
- [49] H. Liu, Q. Zhang, C. Gu, H. Su, V.C. Li, Influence of micro-cracking on the permeability of engineered cementitious composites, *Cem. Concr. Compos.* 72 (2016) 104–113.
- [50] R. Ranade, J. Zhang, J.P. Lynch, V.C. Li, Influence of micro-cracking on the composite resistivity of engineered cementitious composites, *Cem. Concr. Res.* 58 (2014) 1–12.
- [51] S.M. Spearing, F.W. Zok, Stochastic aspects of matrix cracking in brittle matrix composites, *J. Eng. Mater. Technol.* 115 (3) (1993) 314–318.
- [52] H.C. Wu, V.C. Li, Stochastic process of multiple cracking in discontinuous random fiber reinforced brittle matrix composites, *International Journal of Damage Mechanics* 4 (1) (1995) 83–102.
- [53] T. Kanda, Z. Lin, V.C. Li, Tensile stress-strain modeling of pseudo strain hardening cementitious composites, *J. Mater. Civ. Eng.* 12 (2) (2000) 147–156.
- [54] B.T. Huang, Fatigue performance of strain-hardening fiber-reinforced cementitious composite and its functionally-graded structures, in: Ph.D. Thesis, Department of Civil Engineering, Zhejiang University, 2018.
- [55] H.L. Wu, J. Yu, D. Zhang, J.X. Zheng, V.C. Li, Effect of morphological parameters of natural sand on mechanical properties of engineered cementitious composites, *Cem. Concr. Compos.* 100 (2019) 108–119.
- [56] ASTM C109/C109M, Standard Test Method for Compressive Strength of Hydraulic Cement Mortars, ASTM International, West Conshohocken, PA, 2013.
- [57] Japan Society of Civil Engineers, Recommendations for design and construction of high performance fiber reinforced cement composites with multiple fine cracks (HPFRCC), in: *Concrete Engineering Series No. 82*, 2008.
- [58] C. Lu, J. Yu, C.K.Y. Leung, An improved image processing method for assessing multiple cracking development in strain hardening cementitious composites (SHCC), *Cem. Concr. Compos.* 74 (2016) 191–200.
- [61] E.H. Yang, S. Wang, Y. Yang, V.C. Li, Fiber-bridging constitutive law of engineered cementitious composites, *J. Adv. Concr. Technol.* 6 (1) (2008) 181–193.
- [62] R. Ranade, V.C. Li, M.D. Stults, T.S. Rushing, J. Roth, W.F. Heard, Micromechanics of high-strength, high-ductility concrete, *ACI Mater. J.* 110 (4) (2013) 375.
- [63] V.C. Li, H. Stang, H. Krenchel, Micromechanics of crack bridging in fibre-reinforced concrete, *Mater. Struct.* 26 (8) (1993) 486–494.